



Minerva Access is the Institutional Repository of The University of Melbourne

Author/s:

Li, Q;Miramini, S;Smith, DW;Gardiner, BS;Zhang, L

Title:

Osteochondral junction leakage and cartilage joint lubrication

Date:

2023-03-01

Citation:

Li, Q., Miramini, S., Smith, D. W., Gardiner, B. S. & Zhang, L. (2023). Osteochondral junction leakage and cartilage joint lubrication. *Computer Methods and Programs in Biomedicine*, 230, <https://doi.org/10.1016/j.cmpb.2023.107353>.

Persistent Link:

<https://hdl.handle.net/11343/332464>

License:

[CC BY](#)

1 **Title: Osteochondral junction leakage and cartilage joint**  
2 **lubrication**

3 **Authors: Qin Li<sup>1</sup>, Saeed Miramini<sup>1</sup>, David W. Smith<sup>2</sup>, Bruce S.**  
4 **Gardiner<sup>3</sup>, Lihai Zhang<sup>1,\*</sup>**

---

<sup>1</sup> Department of Infrastructure Engineering, The University of Melbourne, VIC, 3010, Australia

<sup>2</sup> School of Physics, Mathematics and Computing, The University of Western Australia, WA, 6009, Australia

<sup>3</sup> Centre for Molecular Medicine and Innovative Therapeutics, Murdoch University, WA, 6150, Australia

\* Corresponding author (Email: [lihzhang@unimelb.edu.au](mailto:lihzhang@unimelb.edu.au))

***Highlights:***

- Effect of osteochondral junction leakage on cartilage tissue lubrication

## 5 **Abstract**

6 **Background and Objectives:** Previous studies have shown that there is potentially interstitial  
7 fluid exchange between cartilage tissue and the subarticular spongiosa region in the case of  
8 injury or disease (e.g., osteoarthritis and osteoporosis). Interstitial flow is also required for  
9 cartilage lubrication under joint load. A key question then is how cartilage lubrication is  
10 modified by increased interstitial fluid leakage across the osteochondral junction. Thus, the  
11 purpose of this study is to develop a numerical model to investigate changes in cartilage  
12 lubrication with changes in osteochondral junction leakage.

13 **Methods:** The multi-phase coupled model includes domains corresponding to the contact gap,  
14 cartilage tissue and subchondral bone plate region (ScBP). Each of these domains are treated  
15 as poroelastic systems, with their coupling implemented through mass and pressure  
16 continuity. The effects of osteochondral junction leakage on lubrication were investigated  
17 with a parametric study on the relative permeability between the ScBP and cartilage tissue.

18 **Results:** Significant effects of ScBP permeability were predicted, especially during the early  
19 stage of the junction leakage development (early stage of the disease). There is a significant  
20 reduction in mixed-mode lubrication duration under the effect of increased junction leakage  
21 (the cartilage tissue mixed-mode lubrication duration is about 33% decrease for a relative  
22 permeability ratio of 0.1 between ScBP and cartilage tissue, and about 52% decrease under  
23 the osteoarthritis condition). In addition, the time for cartilage to reach steady-state  
24 consolidation is significantly reduced when ScBP permeability increases (the consolidation  
25 time reduces from roughly 2 hours to 1.2 hours when the relative permeability ratio increases  
26 from 0.001 to 0.1, and it reduces to 0.8 hours for an advanced osteoarthritis condition). It is  
27 predicted that the initial friction coefficient could increase by over 60% when the ScBP  
28 permeability is consistent with an advanced osteoarthritis (OA) condition.

29 **Conclusion:** Increased osteochondral junction leakage induced by joint injury and disease  
30 could result in increased cartilage surface wear rates due to more rapid interstitial fluid  
31 depressurization within articular cartilage.

32

33 **Keywords:** Cartilage; subchondral bone plate region; osteochondral junction leakage;  
34 coefficient of friction; mixed-mode lubrication duration; permeability

## 35 **1 Introduction**

36 Friction force is defined as the resistance to the relative motion between two opposing  
37 surfaces. It can be the dry friction between solid components or the fluid friction caused by  
38 shear of viscous fluids, while in the case of saturated porous solids there is some combination  
39 of the two (*i.e.*, known as 'mixed mode'). In the context of articular cartilage, mixed mode  
40 lubrication usually occurs in the synovial joints between opposing cartilage surfaces [1, 2].

41 Articular cartilage [2], within the knee synovial joint, is a thin biological soft tissue covering  
42 the end of the tibia and femur bone where it exhibits the extraordinary characteristic of a  
43 bearing material with an ultra-low initial friction coefficient of 0.001. This outstanding  
44 lubrication outperforms the most slippery materials in the world, such as boron-aluminum-  
45 magnesium (0.02 of the friction coefficient [3]) and Teflon (0.05 of the friction coefficient [4]).  
46 The cartilage lubrication mechanisms have been studied extensively over the past decades  
47 and many theories have been proposed [5, 6]. These theories include fluid-film lubrication [7],  
48 mixed-mode lubrication [1, 8], boundary lubrication [9], biphasic lubrication [10] and weeping  
49 lubrication [11, 12] amongst others [5].

50 Synovial joints experience an ultralow friction coefficient at the early stage of mixed mode  
51 lubrication regime due to the pressurized interstitial fluid in the cartilage tissue; this  
52 mechanism is referred to as hydrodynamic lubrication. Under loading, the fluid exudes from  
53 the cartilage tissue resulting in load sharing between solid and fluid phases. This addition of  
54 solid-solid contact, or asperity contacts, leads to both hydrodynamic and boundary  
55 lubrication, and is known as mixed mode lubrication [2]. The mixed-mode lubrication duration  
56 in this paper is defined as the time between the initial contact of the cartilage surface  
57 asperities and 99% depletion of the gap fluid (*i.e.*, when the gap fluid pressure due to joint  
58 loading approaches to zero) [1].

59 Cartilage tissue normally has extremely low fluid permeability. However, the subchondral  
60 bone plate region (ScBP), which is defined as the subchondral cortical bone plate, in the  
61 canalicular region immediately beneath the cement line, including the calcified cartilage layer  
62 in this study, has a (microscale) permeability that is significantly smaller than articular  
63 cartilage under normal conditions. The calcified cartilage is the deep zone cartilage tissue that  
64 has a solid fraction comprising calcium crystals and collagen fibrils. The calcium crystals are  
65 essentially watertight, and the collagen fibrils have low permeability, and together they help

66 to create an impermeable or near-impermeable osteochondral boundary. This subchondral  
67 bone plate region (ScBP) is generally believed to be impermeable [13-16] for normal and  
68 healthy joints. Even though this concept has been challenged recently [17, 18], some studies  
69 still show that the impermeable or near-impermeable assumption is a good approximation  
70 for healthy young adult joints in the numerical modelling [19-23].

71 The studies from Martin-badosa et.al. [19] and Schneider et.al. [20, 21] suggests that the  
72 vascular porosity in femur cortical bones is found to be in the range of  $\sim 1 - 5 \%$ , but this  
73 vascular porosity value includes the Haversian and Volkmann canals. However the  
74 subchondral bone plate region that is immediately beneath the cement line has canalicular  
75 porosity only, so the porosity value should be around the lower end of this range in normal  
76 adult subchondral bone (i.e. in the region of less than 1% to 2%). Similarly from Pouran's  
77 measurements [22], the porosity in human chondral bone plate can be as low as 4% in elderly  
78 people (aged between 67 to 85), this value considers the possible aging effect on the bone  
79 density and the pores space arising from new Haversian and Volkmann canals, which  
80 obviously results in a porosity higher than that of the canalicular systems alone (the region  
81 that is immediately beneath the cement line).

82 Malandrino et. al. [23] proposed an empirical relationship between porosity and permeability.  
83 If we assume a porosity of 1% (in young and healthy adult's joint) for the subchondral bone  
84 plate region (excluding the Haversian and Volkmann canals region), we can estimate ScBP  
85 permeability being about  $3.3 \times 10^{-19} \text{ m}^4/\text{Ns}$  according to their empirical relationship [23],  
86 this is about 3 to 4 orders of magnitude smaller than cartilage tissue's permeability. This  
87 theoretical calculation is also consistent with Gailani et al's experimental results [24] (which  
88 suggests a even lower permeability, around  $10^{-20} \text{ m}^4/\text{Ns}$ ). In addition theoretical calculation  
89 confirm these low permeability estimates. Given the thickness of the subchondral bone with  
90 canalicular porosity only immediately beneath the subchondral cement line and its  
91 exceptionally low permeability, as well as the thickness of the calcified cartilage layer with a  
92 reduced permeability, it is then reasonable to assume the impermeable or near-impermeable  
93 condition for osteochondral junction region for normal adult joints.

94 However, the impermeable (or nearly impermeable) assumption is unlikely to be accurate for  
95 older people, particularly those with osteoarthritic joints. As shown in Hwang's experiment  
96 [25], in the osteochondral junction of patients with the average age of 70 years old requiring

97 arthroplasty due to OA, the permeability in the subchondral bone plate region (cortical bone  
98 plate plus CCZ) is at least 350 – 600 times greater than the permeability of the hyaline cartilage  
99 tissue itself [25]. Even larger increases, of several orders of magnitude has been reported for  
100 increases in vertebral end-plate permeability with age [26]. Together these findings suggest  
101 that the impermeable boundary condition at the osteochondral junction is probably  
102 inaccurate in aged and especially in joints with advanced osteoarthritis [17]. We therefore  
103 consider fluid leakage through the osteochondral junction as a result of aging and/or disease  
104 states, and its effect on joint lubrication.

105 Increased fluid leakage at the osteochondral junction may compromise cartilage lubrication  
106 at the contacting surfaces, as osteochondral leakage provides an extra drainage pathway as  
107 the articular cartilage consolidates, and also reduces the drainage path length, so again  
108 increasing the cartilage tissue drainage rate. Consequently tissue deformation and the  
109 depletion of the elevated pressurized fluid occurs more quickly when osteochondral junction  
110 leakage increases. The additional flow path will result in less fluid escaping via the contact  
111 gap, which will reduce the effect of so-named ‘weeping lubrication’, as proposed by  
112 McCutchen et al. [11, 12]. Reduced lubrication reduces the time that the tissue is able to  
113 sustain the physiological loading without significant cartilage surface friction, which then  
114 leaves the cartilage surface more susceptible to damage.

115 This paper serves as the first step toward coupling the osteochondral junction region with the  
116 cartilage tissue, and cartilage contact gap, to improve our understanding of the role  
117 subchondral bone plate permeability plays in cartilage lubrication within synovial joints. The  
118 objective of this study is to numerically investigate the effect of the permeable subchondral  
119 bone plate on cartilage lubrication behavior under osteochondral junction leakage conditions.  
120 We hypothesize that once the subchondral bone plate becomes more permeable, the  
121 lubrication capability of the cartilage tissue will deteriorate significantly. To test this  
122 hypothesis, we develop a mathematical model to simulate the lubrication and consolidation  
123 behavior of the cartilage tissue, and use the model to predict the critical parameters in  
124 cartilage lubrication including the mixed-mode lubrication duration, time-dependent peak  
125 strain, degree of consolidation, and the time-dependent friction coefficient. The friction  
126 coefficient used in this paper is the effective friction coefficient [27], which varies depending  
127 on the fluid load support. At the early stage of loading, the joint load is supported by the

128 pressurized fluid in the cartilage tissue resulting in minimum solid contact and very low  
129 friction; however when the pressurized fluid drains away, the solid component of the  
130 opposing cartilage tissues starts making more contacts and the effective friction coefficient  
131 then rises. In prior studies it is shown that the effective friction coefficient could reach around  
132 0.3 at an equilibrium steady-state [27].

## 133 **2 Materials and methods**

### 134 **2.1 Study overview and assumptions**

135 This study presents a multi-phase coupled model of the joint under the mixed-mode  
136 lubrication regime. The model incorporates the fluid flow behavior in different regions and  
137 also the fluid interactions between these regions under physiological loading, as listed below:

- 138 • Fluid flow in the cartilage contact gap, interstitial fluid flow in the cartilage tissue, and  
139 interstitial fluid flow through the subchondral bone plate
- 140 • Fluid exchange between the contact gap and cartilage tissue, and fluid exchange  
141 between the cartilage tissue and subchondral bone plate

142 The contact gap model [1] considers the gap fluid flow based on gap permeability and surface  
143 asperity deformation during gap closure with fluid exchange between tissue and contact gap.

144 The cartilage tissue model [28] considers the fluid flow based on Darcy's Law. The subchondral  
145 bone plate model considers the fluid flow based on Darcy's Law, with permeability of the  
146 subchondral cortical bone  $K_{SCBP}$  being a portion of the cartilage tissue permeability  $K_c$ .

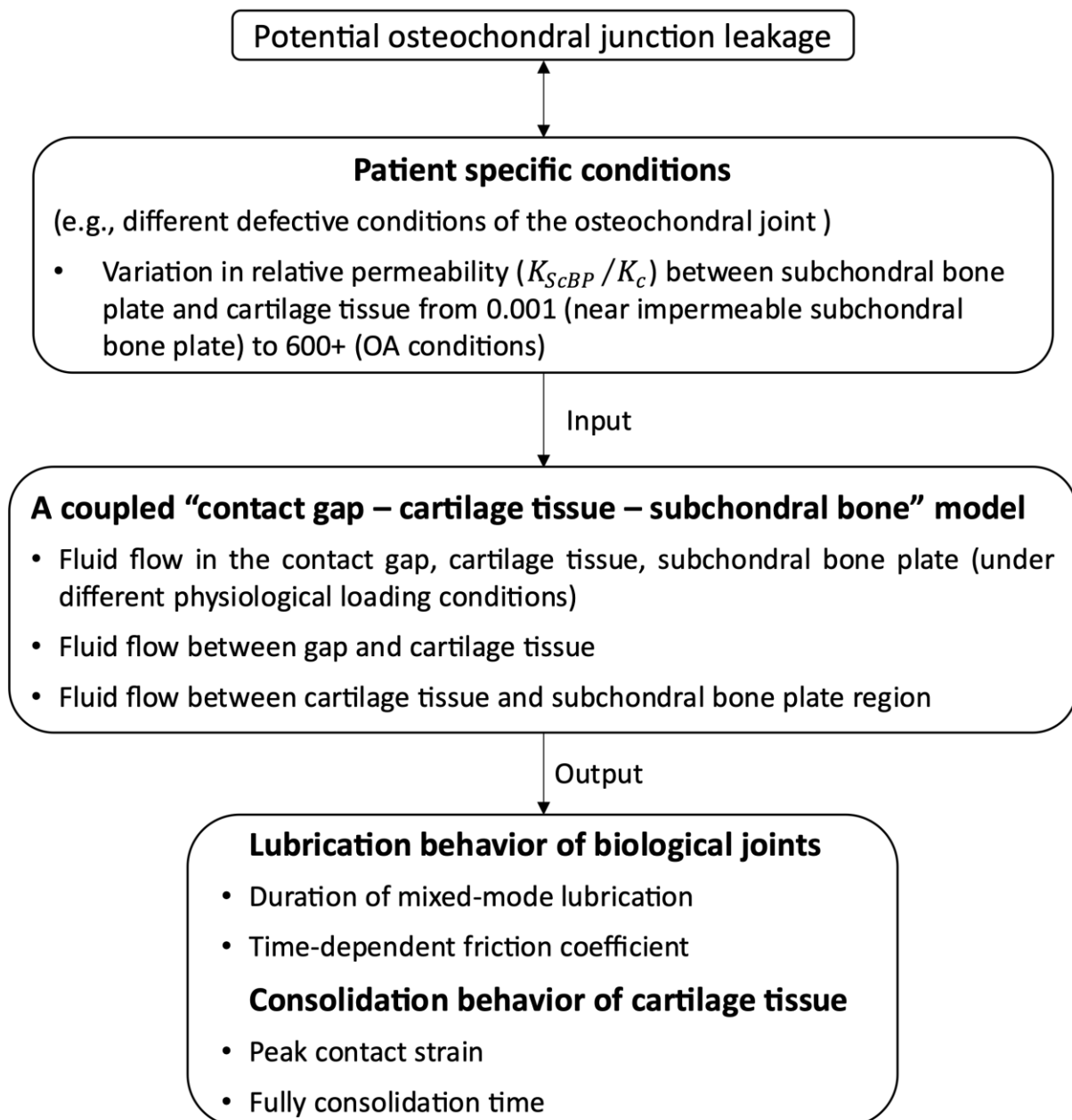
147 In this study, we aim to investigate the effect of the potential for a defective osteochondral  
148 junction to influence tissue lubrication at the contacting surfaces, by increasing the relative  
149 permeability of the subchondral bone plate from a normal condition (with a near  
150 impermeable state,  $K_{SCBP}/K_c = 0.001$ ) towards the advanced OA condition ( $K_{SCBP}/K_c \rightarrow$   
151 600) [2, 25].

152 An overview of this study and the methodology is presented in figure 1, the schematic  
153 diagram showing the details of the model is given in figure 2. The model is constructed under  
154 the cylindrical coordinate system. Note that the cartilage tissue, cartilage contact gap, and  
155 subchondral bone plate are all considered as biphasic porous media and coupled in the joint  
156 lubrication system model.

157 The main assumptions that were used in the study are summarized as follows.

- 158 • An axis-symmetrical geometry and boundary conditions is assumed. This assumption  
159 has also been adopted in previous studies [1, 29, 30].
- 160 • An axis-symmetric coordinate is adopted, meaning that the load distribution, stress-  
161 strain response, and fluid flow behaviour will be the same in all directions in this model.  
162 It is a reasonable assumption due to the shape of the meniscus [31], and the  
163 approximately axisymmetric strain contours observed by Marzo and Gurske-DePerio  
164 under a controlled experimental condition [32].
- 165 • The viscosity, density, and molecular composition of synovial fluid and cartilage  
166 interstitial fluid is assumed to be unchanged throughout the simulation.

167



168

169

**Figure 1: Schematic diagram showing the methodology used in this study**

170

## 171 **2.2 Joint multi-phase coupled model**

### 172 **2.2.1 Cartilage tissue poroelastic model**

173 The authors previously published and developed the cartilage tissue model based on an  
174 upscaled porous media theory [28-30, 33], which was validated against the *in vitro*  
175 experimental measurement [34]. The use of the porous media theory to predict cartilage

176 mechanical response is not a recent idea [35, 36], however its use to couple with cartilage  
 177 contact gap and subchondral bone plate to form a osteochondral joint is relatively new.

178 Under this poroelastic theory framework, the cartilage model [28-30] incorporates the  
 179 aggrecan-dependent tissue stiffness, tension-compression nonlinearity [37] and aggrecan-  
 180 dependent permeability. The cartilage in the model is treated as a fully saturated porous  
 181 media that has the interstitial fluid phase and solid phase (extracellular matrix) [2, 38-40].

182 For the force balance in the cartilage tissue model, the conservation of momentum is applied  
 183 by neglecting the body and inertia forces as shown below [2, 29, 30],

$$\nabla \cdot \boldsymbol{\sigma}_t = 0 \quad (1)$$

184 where  $\boldsymbol{\sigma}_t$  is the total stress (cauchy stress tensors of solid and fluid) in the cartilage, given by  
 185 [27, 30, 36],

$$\boldsymbol{\sigma}_t = \boldsymbol{\sigma}_{solid} + \boldsymbol{\sigma}_{fluid} = \boldsymbol{\sigma}_E^S - p_c \mathbf{I} \quad (2)$$

186 where  $\boldsymbol{\sigma}_E^S$  is the incremental elastic effective stress of the deformed solid phase under loading,  
 187 and  $p_c$  is the incremental interstitial fluid pressure, and  $\mathbf{I}$  is the identity tensor.

188 The solid phase constituent effective stress  $\boldsymbol{\sigma}_E^S$  is given below [30],

$$\boldsymbol{\sigma}_E^S = \frac{2}{J^S} \mathbf{F}^S \cdot \frac{\partial U(\mathbf{u}^S)}{\partial \mathbf{C}^S} \cdot \mathbf{F}^{ST} \quad (3)$$

189 where  $U(\mathbf{u}^S)$  is the stored Helmholtz energy per unit volume (i.e., strain energy density) [41],  
 190 and  $\mathbf{F}^S$  is deformation gradient, and  $\mathbf{C}^S = \mathbf{F}^{ST} \times \mathbf{F}^S$  is right Cauchy-Green solid deformation  
 191 tensor, and  $J^S = \det(\mathbf{F}^S)$  is the volume change ratio.

192 The tension-compression nonlinearity of the solid matrix is considered in the model by  
 193 employing the Conewise Linear Elasticity model with different tensile and compressive  
 194 properties [37, 42]. The aggrecans with glycosaminoglycans of high fixed charge density  
 195 induce high osmotic pressure, and hence contributing to tissue compressive stiffness under  
 196 the load [27, 43]. The relationship between cartilage solid matrix compressive stiffness and  
 197 aggrecan is given below based on the experimental studies [44].

$$H_A = \alpha_1 \phi_G + \alpha_2 \phi_G^2 \quad (4)$$

198 where  $H_A$  is the aggregate (osmotic) modulus,  $\alpha_1 = 0.01 \text{ MPa}$  and  $\alpha_2 = 0.075 \text{ MPa}$  are the  
 199 empirical constants [44],  $\phi_G$  is the “actual” aggrecan concentration with respect to the  
 200 cartilage volume excluding the collagen volume fraction.

201 The “actual” aggrecan concentration  $\phi_G$  varies with cartilage deformation and location, as  
 202 given below

$$\phi_G = \frac{\phi_{G0}}{J^s - CVF} \quad (5)$$

203 where  $\phi_{G0}$  is the depth-dependent initial “apparent” aggrecan concentration with respect to  
 204 initially total cartilage volume (the values are linear interpolated between  $\phi_{G0}|_{z=0} =$   
 205  $30 \text{ mg/ml}$  and  $\phi_{G0}|_{z=5\text{mm}} = 120 \text{ mg/ml}$  [1, 45], where  $z = 0$  represents the center line of  
 206 cartilage surface toughness as presented in figure 2),  $CVF$  is the depth-dependent collagen  
 207 volumetric fraction (45% at superficial zone, 30% at the middle zone, 25% at deep zone) [29].

208 The cartilage tissue compressive elastic modulus ( $E_c$ ) [2] can then be calculated from the  
 209 aggregate modulus as shown below

$$E_c = 3H_A(1 - 2\nu) \quad (6)$$

210 where  $\nu$  is aggrecan effective poisson ratio.

211 The tensile stiffness of cartilage matrix ( $E_t$ ) that is governed by the collagen network exhibits  
 212 depth-dependent and orientation-dependent features, the values adopted in this study is  
 213 summarized in below table [29, 46].

214 **Table 1 – tensile modulus and shear modulus for cartilage [29, 46]**

	Tensile modulus (Mpa)		Shear modulus (Mpa)
	Horizontal	Vertical	
Superficial zone	100	25	3
Middle zone	30	10	3
Deep zone	10	6	2

215  
 216 As mentioned previously, a non-linear tension-compression material model is used in the  
 217 computational model to describe cartilage tissue deformation behaviour. Therefore,  $E_c$   
 218 describes cartilage’s modulus of elasticity in compression, whereas  $E_t$  describes cartilage’s  
 219 modulus of elasticity in tension. Both  $E_c$  and  $E_t$  are implemented in the stiffness matrix in

220 the computational model, so that when a sepcific element of the tissue is under tension,  $E_t$   
 221 will be applied in the deforamtion calculation; and once when the specific element is under  
 222 compression,  $E_c$  will be incorporated.

223 The fluid flow in the cartilage is governed continuity equation (mass conservation) and Darcy's  
 224 law [47-51],

$$\nabla \cdot (\mathbf{v}_d^c + \mathbf{v}_s) = 0 \quad (7)$$

$$\mathbf{v}_d^c = \phi_f (\mathbf{v}_f - \mathbf{v}_s) = -K_c \nabla p_c \quad (8)$$

225 where  $\mathbf{v}_d^c$  the fluid flux is referred to as the Darcy's velocity of the fluid within the tissue  
 226 defined as the relative velocity between fluid phase  $\mathbf{v}_f$  and solid phase  $\mathbf{v}_s$ .  $\phi_f$  the porosity is  
 227 taken as 0.8 [52].  $K_c$  is the aggrecan dependent permeability, which takes into account of the  
 228 effect of the negative charged ions on flow resistance, the empirical equation is given below  
 229 based on the experimental observations [53, 54].

$$K_c = \frac{n \cdot (\phi_G)^m}{\eta_c} \quad (9)$$

230 where  $n = 5.4e-22 \text{ m}^2$  and  $m = -2.37$  are empirical constants.  $\eta_c$  is the water viscosity at 37°C  
 231 (0.0007 Pa · s).

## 232 **2.2.2 The contact gap model**

233 Authors previously developed the contact gap model and coupled it with the above cartilage  
 234 tissue model, and it has been proved that this coupled model represents a more realistic joint  
 235 in the mixed mode lubrication regime when the cartilage is loaded [1]. The modelling is briefly  
 236 descripted below.

237 The model treats the contact gap as a porous medium that consists of gap fluid phase and  
 238 solid phase (the interconnected pores formed by surface roughness between tibial and femur  
 239 cartilage).

240 The fluid flow in the contact gap is governed by Darcy's law,

$$\mathbf{v}_d^g = -K_g \nabla p_g \quad (10)$$

241 where  $\mathbf{v}_d^g$  is the fluid velocity.  $p_g$  is the gap fluid pressure.  $K_g$  is the gap permeability, which  
 242 is dominately determined by the gap height, surface roughness and surface aggrecan. The gap

243 permeability reduces as the gap is closing under the loading, and approaches to cartilage  
 244 permeability when the gap is “functionally closed” (when gap height is about  $1 \mu m$ ) [1]. The  
 245 values for gap permeability have been numerically evaluated based on the computational  
 246 fluid dynamics model against the experimentally measured bovine cartilage surface  
 247 roughness, the details can be found in previous studies [1, 55].

248 The fluid flows, fluid exchange (between contact gap and cartilage tissue) and gap  
 249 deformation (surface asperity and gap size) are governed by the mass conservation,

$$\frac{\partial \varepsilon_v^g}{\partial t} + \nabla \cdot v_d^g = s \quad (11)$$

250 where  $s$  is the rate of change of the fluid exchange per unit volume,  $\frac{\partial \varepsilon_v^g}{\partial t}$  is the rate of change  
 251 of contact gap volumetric strain, the volumetric strain of the contact gap is related to the gap  
 252 height  $h$ , the constitutive relationship for the gap height  $h$  and total stress  $\sigma_t$  was proposed  
 253 based on experimental studies for the human cartilage [56, 57].

$$h = h_0 e^{\sigma_c/\beta} = h_0 e^{\sigma_T + p_g/\beta} \quad (12)$$

254 where  $h_0 = 9 \mu m$  is the undeformed gap height at the beginning of the loading,  $\sigma_c$  is the  
 255 surface asperity contact stress,  $\sigma_T = \sigma_c - p_g$  is the total applied stress which is resisted by  
 256 the solid contact stress ( $\sigma_c$ ) and fluid pressure in the gap ( $p_g$ ),  $\beta$  is the stiffness for the  
 257 cartilage surface asperity (taken as 20% of the aggregate modulus) [1, 58].

258 By integrating the mass conservation equation with the above equations, the governing  
 259 equation at the contact gap in cylindrical coordinates can be obtained as below [1],

$$\frac{1}{\beta} \frac{dp_g}{dt} = \frac{\partial}{\partial r} K_g \frac{\partial p_g}{\partial r} + \frac{K_g}{r} \frac{\partial p_g}{\partial r} + \frac{u_{dv}^c}{h_0 e^{(\sigma_t + p_g)/\beta}} \quad (13)$$

260 where  $u_{dv}^c$  is the normal component of fluid velocity within the cartilage at the interface  
 261 between contact gap and cartilage tissue.

### 262 **2.2.3 The subchondral bone plate model**

263 The subchondral bone plate is modelled as another layer of porous medium underneath the  
 264 cartilage tissue model by considering different material properties as compared to cartilage  
 265 tissue.

266 The continuity equation in the region is given as,

$$\nabla \cdot (\mathbf{v}_f^{scbp} + \mathbf{v}_s) = 0 \quad (14)$$

267 where  $\mathbf{v}_f^{ScBP}$  is Darcy's velocity in the subchondral bone plate,

$$\mathbf{v}_d^{ScBP} = -K_{ScBP} \nabla p_{ScBP} \quad (15)$$

268 where  $K_{ScBP}$  is the ScBP permeability which is taken as a portion of cartilage tissue  
269 permeability in the current study,  $\nabla p_{ScBP}$  is the pressure gradient.

270 The momentum equation is given as

$$\nabla \cdot \boldsymbol{\sigma}_t = 0 \quad (16)$$

271 The total stress  $\boldsymbol{\sigma}_t$  is supported by both the solid and fluid component,

$$\boldsymbol{\sigma}_t = \boldsymbol{\sigma}_{solid} + \boldsymbol{\sigma}_{fluid} = \boldsymbol{\sigma}_E^{ScBP} - p_{ScBP} \mathbf{I} \quad (17)$$

272 The constitutive relation for the solid component in the ScBP region is,

$$\boldsymbol{\sigma}_E^{ScBP} = E_{ScBP} \cdot \boldsymbol{\varepsilon} \quad (18)$$

273 where  $E_{ScBP}$  is the Young's modulus,  $\boldsymbol{\varepsilon}$  is the vertical strain, the deformation of this region is  
274 assumed to be elastic due to the large bone stiffness and relative small physiological load as  
275 compared to the strength, 1-D deformation is considered due to the relative small ScBP  
276 thickness [17, 59, 60] as compared to its cross sectional area. In fact, as expected the  
277 deformation in the bone is very small (negligible) as per calculation, hence any changes in the  
278 bone porosity with loading can be reasonably neglected in the analysis, we note that the other  
279 uncertainties such as the ScBP bone permeability is far more important in the study.

280 To show how the increasing ScBP permeability affects the lubrication behavior of the whole  
281 joint system, a parametric study has been performed, varying the subchondral layer from  
282 being an near impermeable barrier ( $K_{ScBP}/K_c = 0.001$ ) to a very permeable and porous layer  
283 with relative permeability ratio larger than 600 ( $K_{ScBP}/K_c > 600$ ). The high permeability case  
284 represents a compromised layer, through injury or disease [2, 25]. The material properties  
285 for the subchondral bone plate model are summarized in Table 2 [22, 61, 62].

286 **Table 2 – Material properties for the subchondral bone plate used in this study [22, 61, 62]**

The Subchondral Bone Plate	
Young's modulus (Mpa)	17,000
Poisson's ratio	0.3
Density (drained) ( $kg/m^3$ )	800
Fluid compressibility (Mpa)	2,300

## 287 **2.3 Modelling configurations and boundary conditions**

### 288 **2.3.1 Model geometry**

289 The geometry of the model that is adopted in this study was based on MRI measurements  
 290 [63]. The ScBP model is constructed below the cartilage tissue, with an assumption of the  
 291 thickness being 0.4 mm, which is taken from Hwang's experimental work[25]. Note, even  
 292 though ScBP thickness varies depending on the location and joint condition [64, 65], the  
 293 simplification of the constant thickness is reasonable for purpose of investigating how varying  
 294 permeability of the subchondral bone plate region affects the cartilage tissue.

### 295 **2.3.2 Loading configuration**

296 The conically-distributed loading is adopted based on the MRI measurements [63] and  
 297 experimental deformation contours [32]. This loading approach was also used in the previous  
 298 study [29]. To simulate human one-leg standing, the static compression force of 970N (by  
 299 assuming 2.59 body weight for a person weighs 75kg [66]) is applied at the loading interface  
 300 for more than 3 hours to achieve equilibrium condition.

### 301 **2.3.3 Contact gap permeability adjustment**

302 As shown in figure 2, multiple fluid flow paths at the contact gap are considered due to the  
 303 presence of the menisci (i.e., one flow path between contact surfaces of femur and tibia  
 304 cartilages, two flow paths between of femur and meniscus and tibial surface and meniscus).  
 305 To account for this, the contact gap permeability in the region where has two flow paths is  
 306 assumed to be doubled as compared to the region that only has one flow path.

$$\text{Gap permeability} = \begin{cases} K_g, & 0 \leq r \leq l_f, \text{ meniscus free region} \\ 2K_g, & l_f \leq r \leq l_f + l_m, \text{ meniscus covered region} \end{cases} \quad (19)$$

### 307 **2.3.4 Boundary conditions and initial conditions**

308 The boundary conditions for the study is summarized in figure 2 B'-B' and figure 3. The total  
 309 stress  $\sigma_t$  is applied on both contact gap and cartilage tissue at the contact gap and tissue

310 coupling interface. The pressure continuity are also imposed at the interface (figure 2 B'-B'  
 311 and figure 3).

$$p_c(r, 0) = p_g(r, 0) \quad (20)$$

312 The continuity of normal fluid velocity  $u_{dv}^c$  is also imposed at the interface which is already  
 313 accounted for in the mass conservation equation (13) in the contact gap model.

314 The zero pressure (ambient fluid pressure) condition is applied at the periphery edge of the  
 315 contact gap.

$$p_g(r = r_0, z = 0) = 0 \quad (21)$$

316 The free flux (ambient fluid pressure) is also applied at the periphery edge of cartilage tissue  
 317 as shown in figure 3.

318 As for the interface between cartilage tissue and subchondral bone plate model, the fluid  
 319 pressure and flux continuity condition is also applied.

$$p_c(r, z = Th(r)) = p_{scBP}(r, z = Th(r)) \quad (22)$$

$$u_d^c(r, z = Th(r)) = u_d^{scBP}(r, z = Th(r)) \quad (23)$$

320 where  $u_d^{scBP}$  is the normal velocity flux at the subchondral bone plate;  $Th(r)$  is the thickness  
 321 of the cartilage tissue as a function of radius, the geometry of the cartilage tissue is  
 322 constructed based on the MRI image [29, 63];

323 The subchondral trabecular bone (spongy bone) that lies below the subchondral bone plate  
 324 is highly porous bone enclosing a lot of space filled with bone marrow [67, 68]. It is assumed  
 325 to be an opened space to the system due to its large void ratio [69]. Therefore, the free flux  
 326 boundary condition is assigned at the bottom edge of the subchondral bone plate, once the  
 327 fluid can pass the subchondral bone plate, the flow resistance will be reduced significantly.  
 328 The subchondral bone plate is assumed to have 0.4 mm of thickness [70].

$$p_{scbp}(r, z = -Th(r) - 0.4) = 0 \quad (24)$$

329 The fixed constraint is imposed at the bottom edge of the subchondral bone plate model.

330 **2.3.5 Initial conditions**

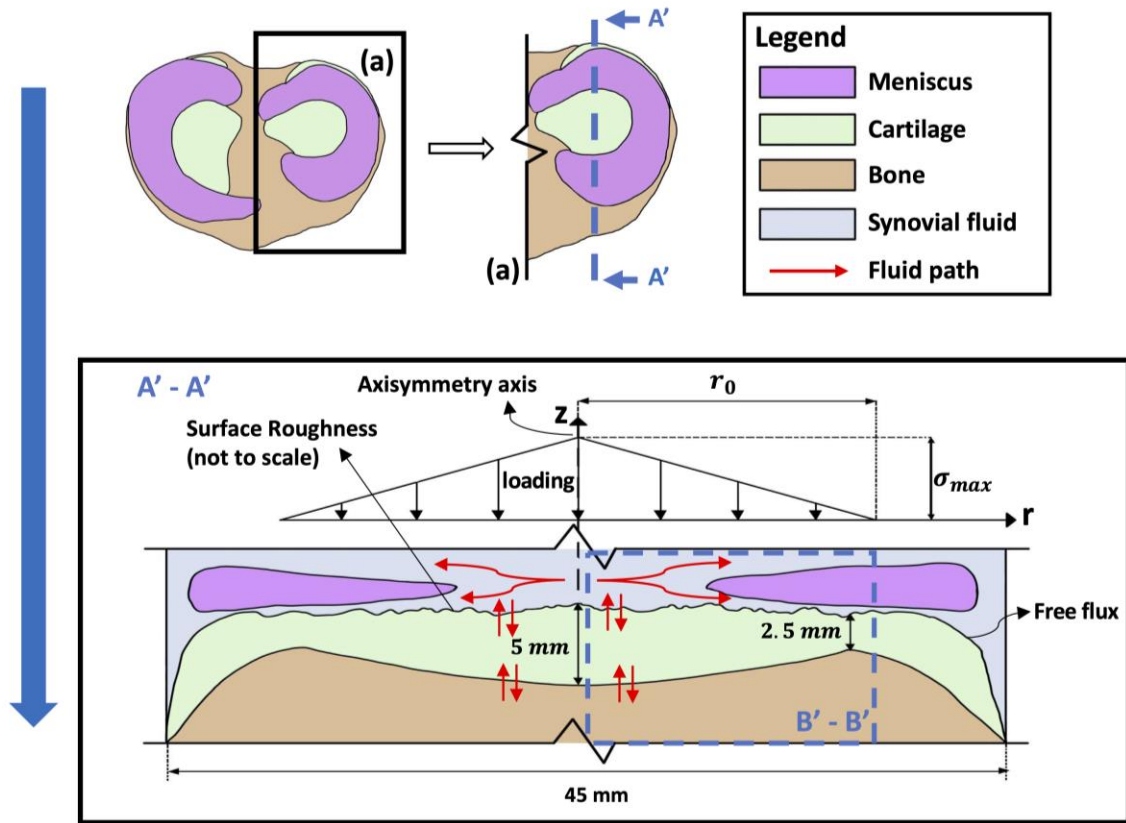
331 The numerical modeling begins with the initial contact of the surface asperities at the contact  
332 gap (for mixed mode lubrication regime). The initial contact gap fluid pressure is assigned as  
333 the total pressure at the cartilage surface (coupling interface).

$$p_g(t = 0) = p_c(t = 0, z = 0) = -\sigma_t; \quad h(t = 0) = h_0 \quad (25)$$

334 **2.4 Numerical model settings**

335 The numerical simulation and finite element analysis are conducted in COMSOL Multiphysics  
336 Poroelastic Module. This multiphase coupled model is constructed as a two-dimensional  
337 axisymmetric model and meshed with 1204 triangle elements. The time-dependent solver  
338 with a general relative tolerance of 0.01 is utilized to solve the governing equations.

339 A few relative permeability cases ( $K_{scbp}/K_{cd} = 0.001, 0.01, 0.02, 0.03, 0.05, 0.1, 0.15, 0.2,$   
340  $0.4, 0.6, 0.8, 0.9, 1, 5, 10, 50, 350, 600, 1000$ ) were considered in this parametric study to  
341 cover the input range.



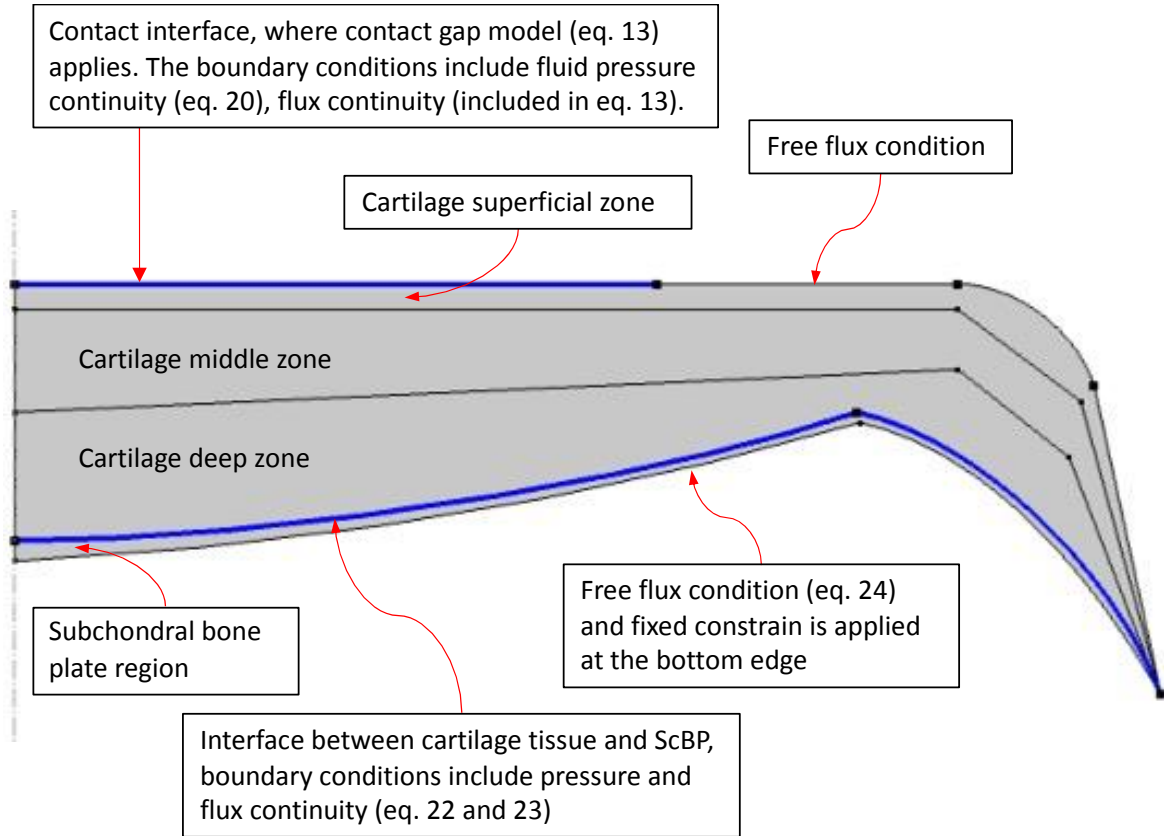
342

343

344

345

Figure 2: Schematic diagram of the current study showing the details of the fully coupled “contact gap – cartilage tissue – subchondral bone” model



346

347

**Figure 3: Boundary conditions applied on the multi-phase model**

348

### 349 **3 Results and discussion**

#### 350 **3.1 Cartilage consolidation and deformation behaviour**

351 Figure 4 presents how different degrees of relative permeability ( $K_{ScBP}/K_c$ ) affect the  
 352 cartilage tissue consolidation response. Figure 4 (a) shows the peak contact strains under  
 353 different scenarios. The peak contact strain in this paper is defined as the maximum  
 354 deformation of the cartilage tissue (along the axisymmetric line at the maximum stress)  
 355 divided by the cartilage thickness as shown in eq. (26).

$$\varepsilon(t) = w(t)/Th \quad (26)$$

356 where  $w(t)$  is time-dependent peak deformation;  $Th$  is the maximum cartilage thickness.

357 At the static state, the peak contact strain for all cases is approaching a constant value of  
 358 around 0.28. This is consistent with the experimental measurements performed by Barker  
 359 and Seedhom [34], who reported the average peak strain of 0.31 with a standard deviation

360 of 0.03 at the medial compartment. At times of 10s and 300s, the numerical simulation  
 361 predicts the peak strain of 0.13 and 0.17 respectively, this is also close to MRI measurements  
 362 [71]. The comparison between numerical modeling and experiment measurements is  
 363 summarized in Table 3.

364 **Table 3 – Comparison of peak contact strain between numerical simulation and**  
 365 **experiment measurements.**

Time (s)	Peak Contact Strain	
	Numerical modeling	Experiment measurements: mean (standard deviation)
10	0.13	0.09 (0.03) [71]
300	0.17	0.13 (0.03) [71]
Steady state	0.28	0.31 (0.03) [34]

366  
 367 As shown in figure 4(a), the cartilage tissue in the diseased joint (i.e. for more permeable  
 368 subchondral bone plate cases) deforms much faster compared to the (normal joint) control.  
 369 This is also illustrated in the consolidation curve over the time, as shown in figure 4(c), which  
 370 indicates that the consolidation time reduces at the higher relative permeability cases. In  
 371 other words, the cartilage system consolidates more quickly and the articular cartilage  
 372 deforms at a faster rate. The degree of consolidation in this paper is defined based on the  
 373 peak contact strain as shown below.

$$DoC(t) = \frac{\varepsilon(t) - \varepsilon_0}{\varepsilon_{steady\ state} - \varepsilon_0} \quad (27)$$

374 In eq. (27),  $\varepsilon(t)$  is the time-dependent peak contact strain,  $\varepsilon_0$  is the initial peak contact strain  
 375 (elastic strain) and  $\varepsilon_{steady\ state}$  is the strain at the steady state. Full consolidation time (i.e.  
 376 steady state) is defined when 99% consolidation is reached.

377 It takes about 2 hours for the control case (near impermeable junction, which it is assumed  
 378 to be the case for healthy young adult) to reach a fully consolidation state (99%). While the  
 379 ScBP permeability increases, this steady state consolidation time reduces. For example, when  
 380 the relative permeability ratio is 0.1, the full consolidation time reduces to 1.2 hours. Whereas,  
 381 when the relative permeability ratio is 600, which is consistent with an OA condition, the full

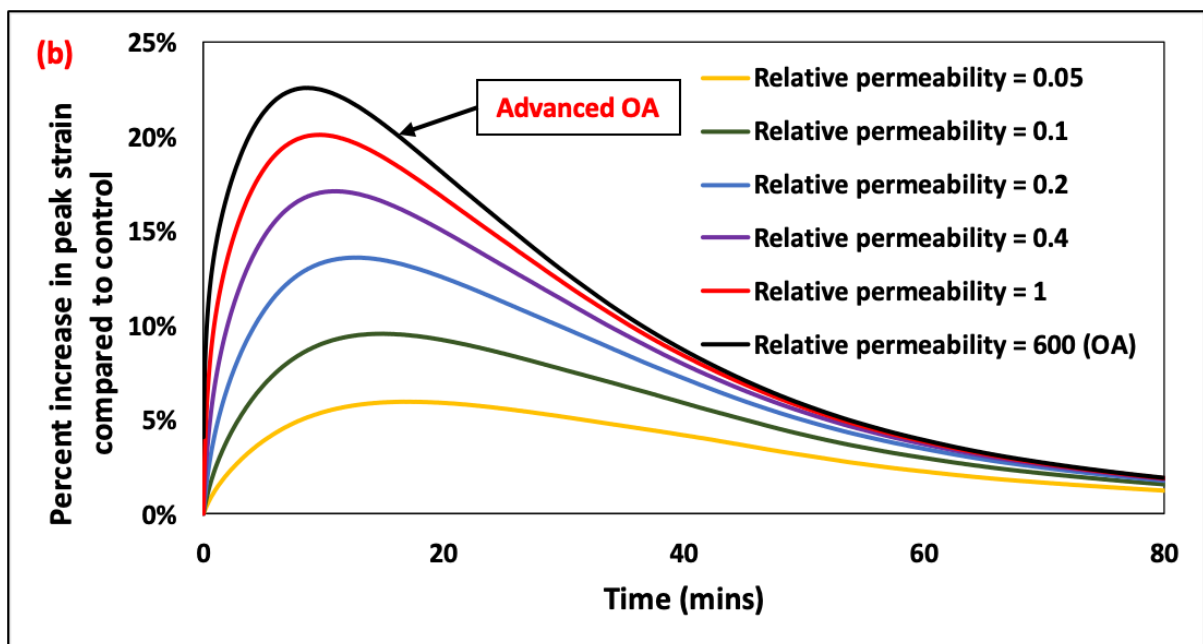
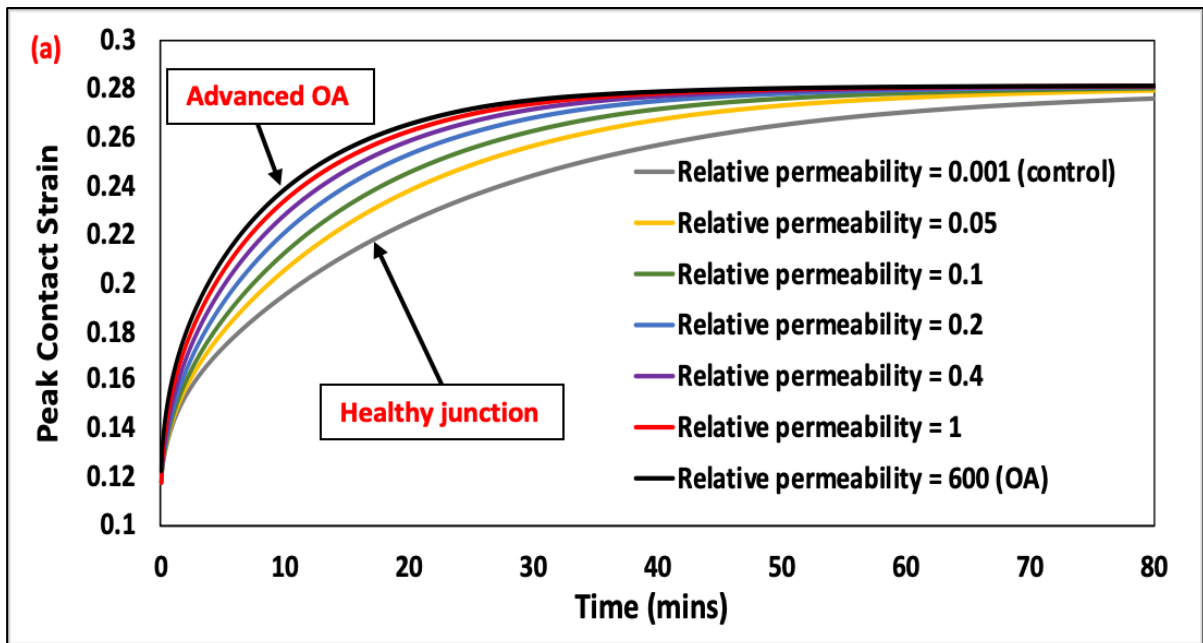
382 consolidaton time reduces further to 0.8 hours, this is about 60% of the reduction as  
383 compared to the control.

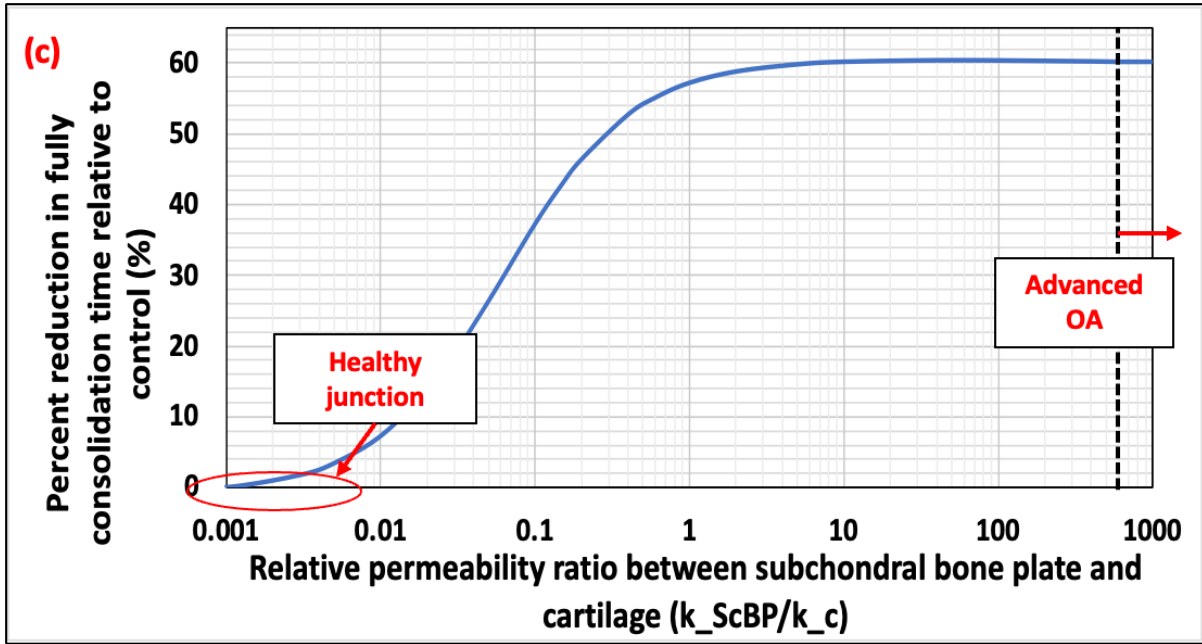
384 Consolidation for the permeable joint (especially for the diseased joint, i.e. OA) is much faster,  
385 as compared to the healthy joint, because of the shorter drainage path (due to the extra  
386 escaping pathway via ScBP), it then leads to a quicker excess pore water depletion, this is also  
387 presented in figure 4 (d) – (f).

388 As the tissue experiences a quicker deformation for higher ScBP permeability, larger  
389 deformations at the early stage of the loading will also occur. As illustrated in figure 4 (b), at  
390 10 mins after the loading, the peak contact strain is 20% higher as compared to the control  
391 for relative permeability ratio of 1, and it is 23% higher under the OA condition when the ratio  
392 is larger than 600 which is very significant. Also, the early stage loading deformation  
393 (percentage increase relative to the control) increases rapidly from 0 to 20% when the  
394 permeability ratio increases from 0.001 to 1. However it only increases from 20% to 23% when  
395 the permeability ratio increases from 1 to 600. It shows that the effect of osteochondral  
396 junction leakage is greater when the relative permeability ratio increases from 0.001 to 1, and  
397 the further increases in ScBP permeability is not promoting any significant effect on the joint  
398 lubrication. Figure 4 (c) also confirms this finding, the reduction in fully consolidation time is  
399 significant for ratio between 0.001 to 1. However the value starts to converge for further  
400 increases of the ScBP permeability.

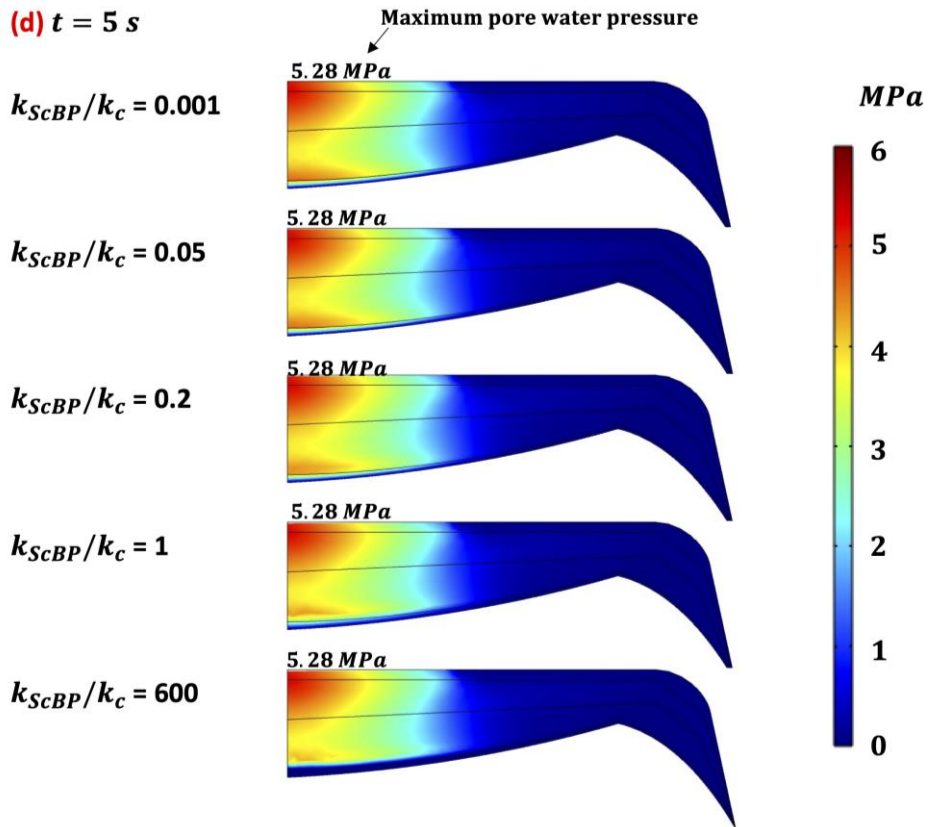
401 Hydraulic pressure throughout tissue increases effectively instantly with the onset of load to  
402 match the load (i.e. the load is initial supported by the fluid in a poroelastic material). Once  
403 leakage at the ScBP starts (when the relative permeability ratio increases from 0.001 to 1),  
404 the built-up pressure within the tissue and the zero-pressure boundary condition (at the  
405 bottome edge of the ScBP) together form a very large pressure gradient, this pressure  
406 gradient will drive fluid out of the tissue via the bone plate, the increase in the permeability  
407 will give more available cross-sectional area for the fluid to escape. The effect of the  
408 increasing ScBP permeability on the tissue deformation and interstitial fluid depresurisation  
409 is significant especially when the relative permeability ratio increases from 0.001 (near  
410 impermeable) to 1 as presented in figure 4. However, as the ratio continues to increase above  
411 1 (in this study), the effect starts to converge and no much further impact was found in the  
412 simulation, which means the impact for the permeable joint on tissue deformation and fluid

413 depurisation is similar between the case when the relative permeability ratio is 1 and 600.  
414 In the physiological condition (i.e. a real joint), it is not exactly clear at which ratio the effect  
415 will converge, because the effect from permeable junction on tissue not only depends on the  
416 ScBP permeability, but also the loading conditions, as different physiological activities can  
417 generate different pressure gradient at the junction (between tidemark and bottom edge of  
418 the ScBP), which can drive the fluid out via ScBP at different rates.

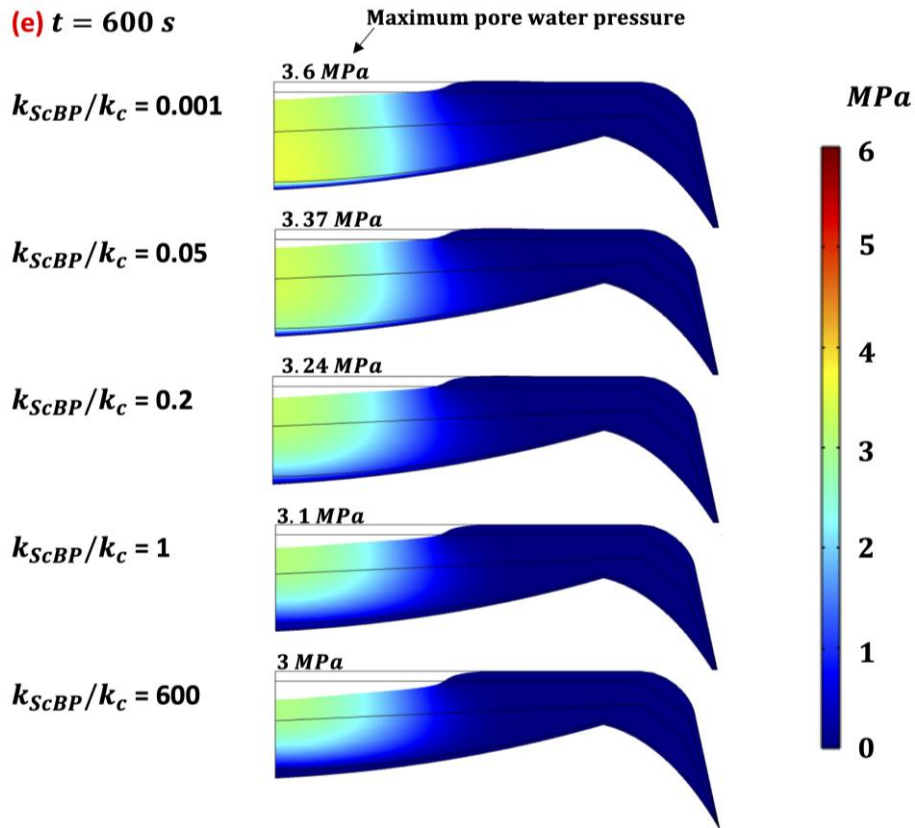




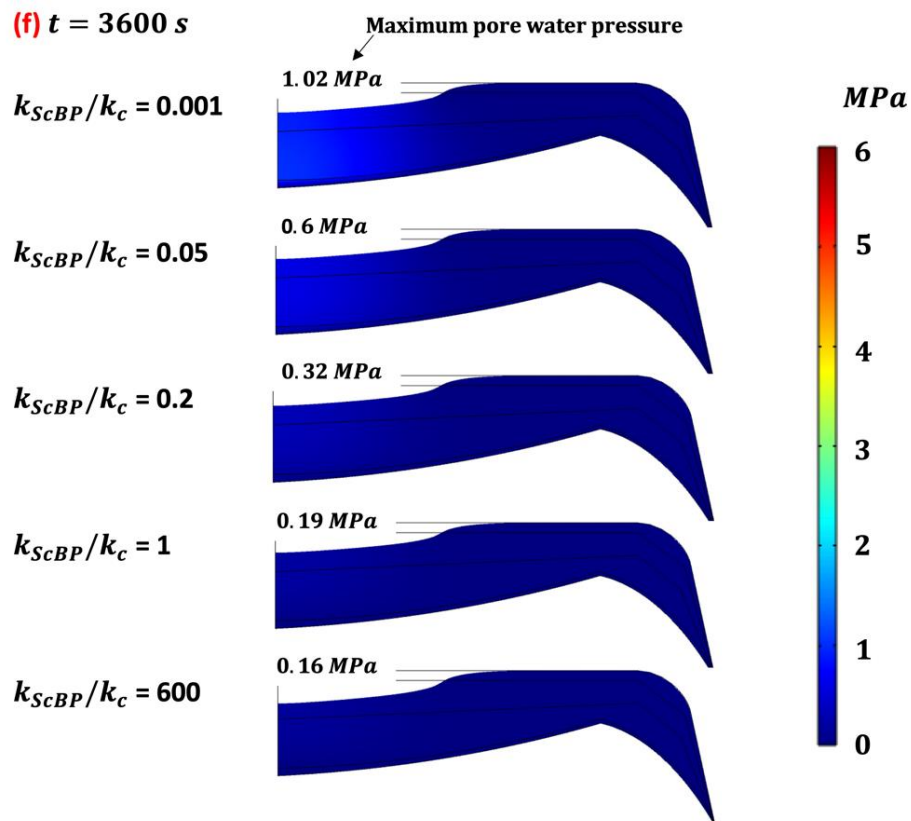
421



422



423



424

425 **Figure 4: (a) Cartilage tissue peak contact strain for different degrees of relative**  
 426 **permeability of subchondral bone ( $K_{ScBP}/K_c$ ); (b) Normalized peak strain for permeable**



## 435 **3.2 Lubrication of the cartilage**

### 436 **3.2.1 Friction coefficient**

437 The time-dependent friction coefficient at the point that has maximum contact stress is used  
438 in this paper to describe the cartilage tissue lubrication behaviour. It is calculated based on  
439 the biphasic lubrication theory [72] and the linear relationship between the degree of  
440 consolidation (DoC) and the effective friction coefficient [29] (eq. (28)),

$$\mu_{eff} = \mu_{eq} \times DoC \quad (28)$$

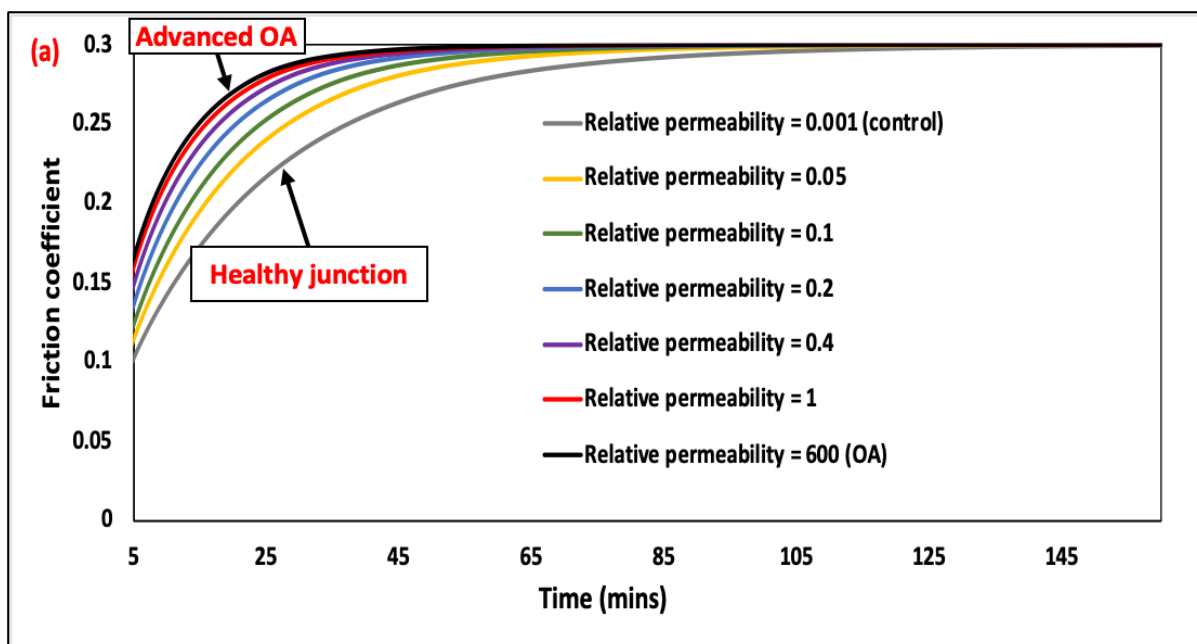
441 where  $\mu_{eff}$  is the time-dependent effective friction coefficient;  $\mu_{eq}$  is equilibrium friction  
442 coefficient which is assumed to be 0.3 [27].

443 Experimental studies suggest that it takes several hours (2-3 hrs) for the cartilage response to  
444 reach the equilibrium under the compressive loading condition (with one end of the cartilage  
445 specimen being impermeable) [27, 73-76]. This timescale is consistent with our modelling  
446 prediction for the healthy and normal joints as presented in figure 5(a). On the other hand,  
447 for the permeable joints, the amount of time required to reach the elevated friction  
448 coefficient is reduced dramatically (by more than half), as compared to the control case.

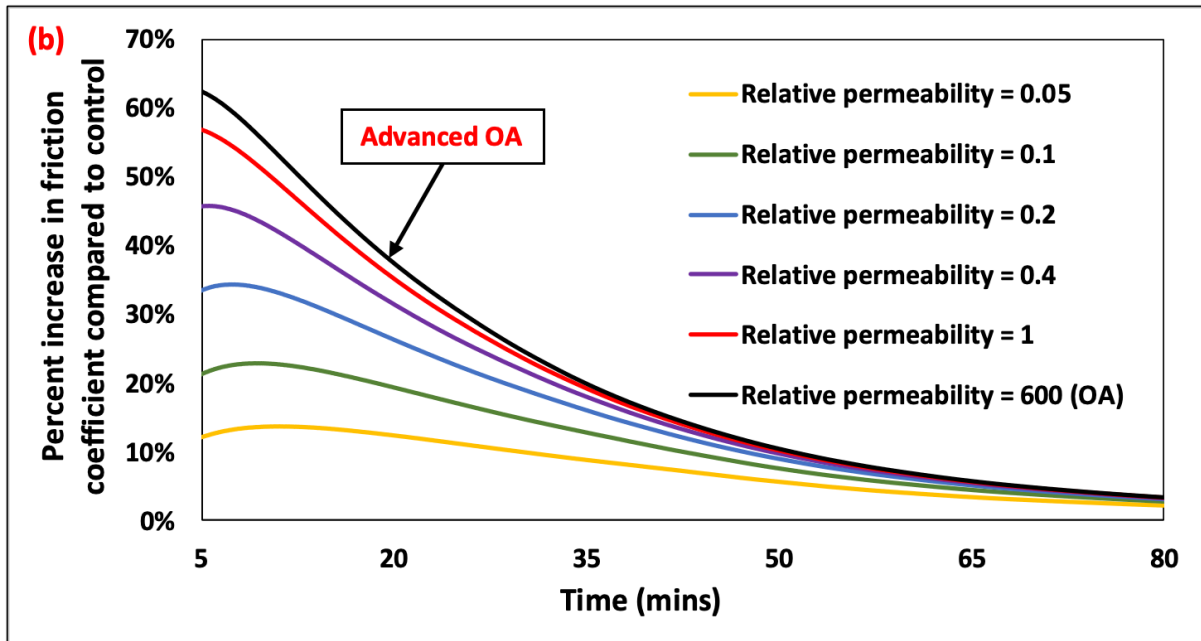
449 The earlier increase in friction in compromised joints is due to the large pressure gradient  
450 between the tide mark and bottom edge of ScBP, in addition to the short drainage path within  
451 the subchondral plate. Once the subchondral bone plate region becomes permeable and  
452 deteriorated, the tissue interstitial fluid will escape quickly via this additional path. With more  
453 fluid escaping through the osteochondral junction, less fluid will remain pressurized at the  
454 superficial layer to resist the applied loading. In addition, the interstitial fluid will be  
455 depressurized at a faster rate due to the smaller flow resistance at the subchondral bone plate  
456 region. Therefore, cartilage solid to solid contact occurs sooner, resulting in the equilibrium  
457 friction coefficient to be reached earlier.

458 At the early stage of the loading (about 5 mins), the friction coefficient for ScBP permeability  
459 at the OA condition is 62% larger than the control, and 57% larger when relative permeability  
460 ratio = 1, and 33% larger when relative permeability ratio = 0.2. This finding indicates the  
461 significance of the osteochondral junction leakage in the development and progression of  
462 osteoarthritis, which is also consistent with the microscopic study performed by Li et al [77],

463 they concluded that the subchondral bone plate that has poorly mineralized and porous bone  
464 is a hallmark of osteoarthritis. It is also widely known that the osteochondral junction is a  
465 dynamic system in the body [2], the subchondral bone continuously remodels according to  
466 the environment (loadings, signals, etc.), the remodelling process cut across the  
467 osteochondral interface, and then potentially leakage happens between cartilage and bone.  
468 Under normal condition, cartilage tissue produces large quantities of OPG to shut down the  
469 bone resorption as the bone remodelling process approaches the cartilage-bone interface and  
470 then blocks the bone remodelling [2, 78-82]. However, as people age or for osteoarthritic  
471 patients, OPG levels in the cartilage falls, and then the bone remodelling may penetrate closer  
472 to the osteochondral interface, and perhaps eventually cross the interface, and lead to the  
473 junction leakage. This may represent a positive feedback loop, i.e., as OA progresses, less OPG  
474 is secreted, promoting more leakage, leading to higher occurrence of high cartilage contact  
475 friction, further promoting the development of the OA.



476



477

478 **Figure 5: (a) Time-dependent friction coefficient under different relative permeability**  
 479 **ratios; (b) Normalized time-dependent friction coefficient for the cases of permeable**  
 480 **osteocondral junction compared to control.**

481

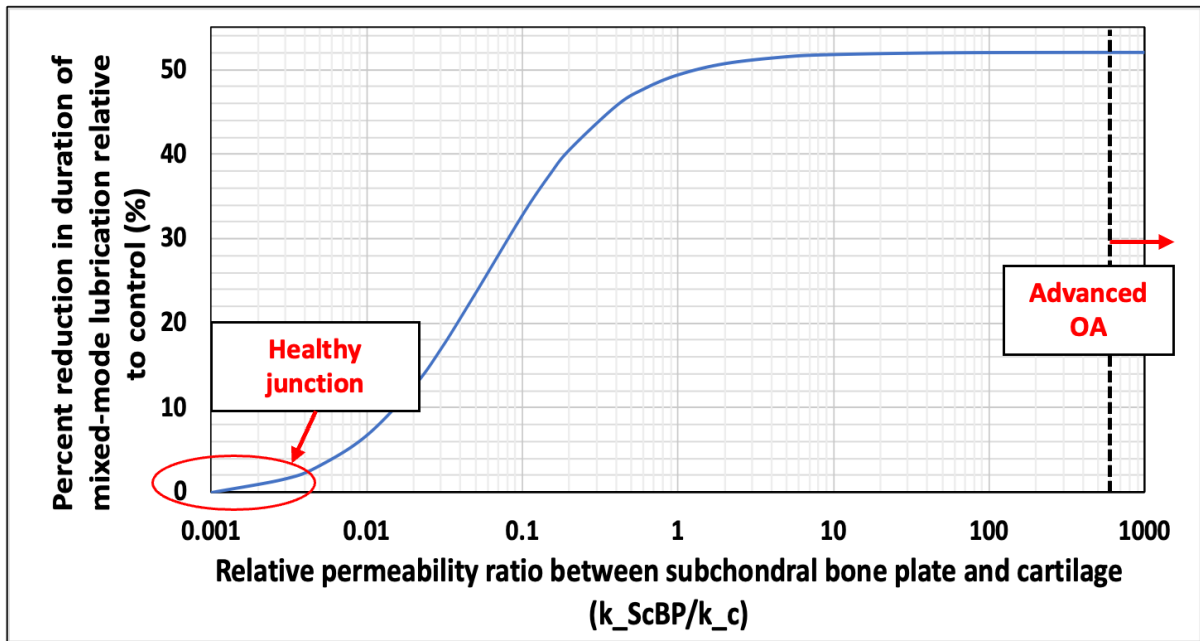
### 482 3.2.2 Mixed-mode lubrication duration

483 Figure 6 shows the normalized mixed-mode lubrication duration as compared to the control.  
 484 As discussed before, mixed-mode lubrication is the joint lubrication regime for most  
 485 physiological activities [8]. It starts when the surface roughness or asperities make contact  
 486 and finishes when the fluid pressure at the contact gap is depleted (when contact gap  
 487 pressure approaches to zero) [1]. It is useful to study the mixed-mode lubrication duration as  
 488 it is an important indicator of joint health. A shorter mixed-mode lubrication duration  
 489 indicates the earlier contact for cartilage solid components, and consequently a higher  
 490 likelihood of cartilage surface wear and osteoarthritis development.

491 This study predicts the mixed-mode lubrication duration of around 160 mins for a healthy  
 492 junction, this is in good agreement with the previous study [29], as it takes several hours for  
 493 the fluid pressurization or friction coefficient to reach an equilibrium value (note, the  
 494 aggrecan-dependent tissue permeability as shown in eq. (9) was adopted in the study with an  
 495 average value across the tissue being  $2.2e-16 m^4/Ns$  at the steady state, this is also  
 496 consistent with the experimental measurements [14, 83]). However, the mixed-mode

497 lubrication duration reduces significantly once the ScBP starts to leak (as shown in figure 6),  
498 the lubrication duration is 33% lower as compared to control when relative permeability = 0.1,  
499 50% lower when relative permeability = 1, and it becomes 52% lower when ScBP permeability  
500 is at OA condition. These results suggest a significant reduction in the knee joint lubrication  
501 capability under the effect of osteochondral junction leakage, as the load that was initially  
502 taken by the fluid is transferred at a faster rate to the solid component of cartilage. When the  
503 osteochondral junction becomes permeable and deteriorated, cartilage interstitial fluid  
504 escapes via ScBP, less available fluid will go into the contact gap to support the mixed-mode  
505 lubrication regime. Together this also reduces the effect of “weeping lubrication” [11, 84]. In  
506 the meantime, the fluid drainage path that comes out of the tissue via the contact gap  
507 interface also becomes shorter, which also contributes to the reduction of the mixed-mode  
508 lubrication duration, and in turn deteriorates the lubrication capability.

509 As discussed in Section 3.1, the effect of osteochondral junction leakage is most significant  
510 when relative permeability is between 0.001 to 1, and further increase in ScBP permeability  
511 only has mild effect. This is also seen in the mixed-mode lubrication duration shown in figure  
512 6, where the joint lubricating capability deteriorates most significantly at the early stage of  
513 the junction leakage development. Further progression only has mild effect and so the tissue  
514 would not deteriorate much further. This finding indicates the importance of early prevention  
515 and intervention of the subchondral bone disease, as once the subchondral bone plate  
516 becomes permeable, the articular joint could suffer significant loss of its lubrication  
517 capability and functionality.



518

519 **Figure 6: Normalized mixed-mode lubrication duration compared to control for different**  
 520 **relative permeability ratios between the subchondral bone plate to cartilage ( $k_{scbp}/k_c$ )**

521

## 522 4 Limitations

523 A few limitations in the study should be noted. First, the current study uses static compressive  
 524 loading to investigate the effect of osteochondral junction leakage on joint lubrication  
 525 behaviour, it serves as the first step in the investigation. In the future study, a dynamic loading  
 526 with different frequencies and speeds (to simulate walking and running) can be used to better  
 527 understand how a diseased osteochondral junction affects the joint. Second, an axis-  
 528 symmetrical geometry and coordinates are employed to simplify the problem. We do expect  
 529 additional variations due to the presence of the meniscus, ligaments, and joint contact  
 530 geometry to also affect the fluid flow behaviour in the gap junction. In future studies,  
 531 improvement can be made by constructing a 3D model of the knee joints based on CT scan  
 532 images to account for these geometrical variables. Third, this study assumes the constant  
 533 synovial fluid viscosity. It is acceptable to adopt for constant value for the static compression  
 534 loading as a first approximation to steady state conditions, however, more complex rheology  
 535 of synovial fluid can be built into the model for a more realistic scenario modelling. Lastly, this  
 536 study estimates the permeability ratio between the subchondral bone plate and cartilage  
 537 based on the subchondral bone plate's porosity. In future studies, improvement can be made

538 by replacing these estimates with experimental data to make these theoretical predictions  
539 closer to reality.

540

## 541 **5 Conclusion**

542 This study investigated the cartilage lubrication but focused on the potential impact of  
543 osteochondral junction leakage. In addition, the effect of the meniscus on fluid flow in the  
544 contact gap was also considered in the modelling. The main conclusions are summarized as  
545 follows:

- 546 • The effect of osteochondral junction leakage is significant on cartilage joint lubrication,  
547 and it is most apparent during the early stage of the junction leakage development  
548 (when relative permeability is between 0.001 to 1.0 in this study).
- 549 • The model predicts that normal adult knee cartilage could take about 2 hours for a  
550 healthy cartilage tissue to reach steady-state consolidation. However, the full  
551 consolidation time reduces to 1.2 hours when relative permeability ratio = 0.1 (early  
552 stage of osteochondral junction leakage). It reduces to 0.8 hours when ScBP  
553 permeability is at the OA condition, this is equivalent to a 60% reduction.
- 554 • The time-dependent friction coefficient rises sooner with the increasing subchondral  
555 bone plate permeability (as the osteochondral junction leakage deteriorates). As  
556 compared to control, the initial friction coefficient increases by 62% for ScBP  
557 permeability at the OA condition, and 57% when relative permeability ratio = 1, and  
558 33% when relative permeability ratio = 0.2. This result indicates the potential for a  
559 significant contribution of a leaky osteochondral junction on the development of knee  
560 diseases, such as osteoarthritis.
- 561 • The mixed-mode lubrication duration and the joint lubrication capability is reduced  
562 significantly when the ScBP becomes permeable (at early stage of osteochondral  
563 junction leakage). As compared to control, the mixed-mode lubrication is 33% lower  
564 when relative permeability = 0.1, and 50% lower when relative permeability = 1, and  
565 it becomes 52% lower when ScBP permeability is at OA condition. These results  
566 suggest a significant reduction in the knee joint lubrication under the effect of  
567 osteochondral junction leakage.

- 568 • Early intervention (*e.g.*, following sports injury) to prevent osteoarthritic subchondral  
569 bone disease may be justified because once the subchondral bone plate becomes  
570 permeable, the articular joint is likely to suffer significant loss in terms of its lubrication  
571 capability, increased wear, and consequent loss of functionality.

572

## 573 **6 Acknowledgements**

574 The authors acknowledge the funding support from The Australian Research Council  
575 (DP180100915) and The University of Melbourne

576

## 577 **7 Conflict of interest**

578 The authors declare that they have no known competing financial interests or personal  
579 relationships that could have appeared to influence the work reported in this paper.

580

## 581 **8 Reference**

- 582 [1] J. Liao, D.W. Smith, S. Miramini, B.S. Gardiner, L. Zhang, A coupled contact model of  
583 cartilage lubrication in the mixed-mode regime under static compression, *Tribology*  
584 *International*, 145 (2020) 106185.
- 585 [2] D. Smith, B. Gardiner, L. Zhang, A. Grodzinsky, *Articular Cartilage Dynamics*, 2019.
- 586 [3] N. Canter, BAM: Antiwear and friction-reducing coating, *Tribology & Lubrication*  
587 *Technology*, 65 (2009) 14.
- 588 [4] D. Flom, N. Porile, Friction of teflon sliding on teflon, *Journal of Applied Physics*, 26 (1955)  
589 1088-1092.
- 590 [5] W. Lin, J. Klein, Recent progress in cartilage lubrication, *Advanced Materials*, 33 (2021)  
591 2005513.
- 592 [6] Z. Jin, J. Fisher, 2 - Tribology in joint replacement\*Note: This chapter is an updated version  
593 of Chapter 2, from the first edition of *Joint replacement technology*, edited by P. A. Revell and  
594 published by Woodhead Publishing, 2008\*, in: P.A. Revell (Ed.) *Joint Replacement Technology*  
595 (Second Edition), Woodhead Publishing 2014, pp. 31-61.
- 596 [7] D. Dowson, V. Wright, M.D. Longfield, Human joint lubrication, *Biomed Eng*, 4 (1969) 160-  
597 165.
- 598 [8] C.P. Neu, K. Komvopoulos, A.H. Reddi, The interface of functional biotribology and  
599 regenerative medicine in synovial joints, *Tissue Eng Part B Rev*, 14 (2008) 235-247.
- 600 [9] M. Daniel, Boundary cartilage lubrication: review of current concepts, *Wien Med*  
601 *Wochenschr*, 164 (2014) 88-94.
- 602 [10] G.A. Ateshian, Biphasic Lubrication, in: Q.J. Wang, Y.-W. Chung (Eds.) *Encyclopedia of*  
603 *Tribology*, Springer US, Boston, MA, 2013, pp. 226-233.

604 [11] P.R. Lewis, C.W. McCutchen, Mechanism of Animal Joints: Experimental Evidence for  
605 Weeping Lubrication in Mammalian Joints, *Nature*, 184 (1959) 1285-1285.

606 [12] C.W. McCutchen, Mechanism of Animal Joints: Sponge-hydrostatic and Weeping  
607 Bearings, *Nature*, 184 (1959) 1284-1285.

608 [13] T.D. Brower, Y. Akahoshi, P. Orlic, The Diffusion of Dyes Through Articular Cartilage in  
609 Vivo, *JBJS*, 44 (1962) 456-463.

610 [14] A. Maroudas, P. Bullough, Permeability of Articular Cartilage, *Nature*, 219 (1968) 1260-  
611 1261.

612 [15] R. Honner, R.C. Thompson, The nutritional pathways of articular cartilage. An  
613 autoradiographic study in rabbits using <sup>35</sup>S injected intravenously, *J Bone Joint Surg Am*, 53  
614 (1971) 742-748.

615 [16] K. Ogata, L.A. Whiteside, Barrier to material transfer at the bone-cartilage interface:  
616 measurement with hydrogen gas in vivo, *Clin Orthop Relat Res*, (1979) 273-276.

617 [17] G. Li, J. Yin, J. Gao, T.S. Cheng, N.J. Pavlos, C. Zhang, M.H. Zheng, Subchondral bone in  
618 osteoarthritis: insight into risk factors and microstructural changes, *Arthritis Research &*  
619 *Therapy*, 15 (2013) 223.

620 [18] X.L. Yuan, H.Y. Meng, Y.C. Wang, J. Peng, Q.Y. Guo, A.Y. Wang, S.B. Lu, Bone-cartilage  
621 interface crosstalk in osteoarthritis: potential pathways and future therapeutic strategies,  
622 *Osteoarthritis Cartilage*, 22 (2014) 1077-1089.

623 [19] E. Martín-Badosa, D. Amblard, S. Nuzzo, A. Elmoutaouakkil, L. Vico, F. Peyrin, Excised  
624 bone structures in mice: imaging at three-dimensional synchrotron radiation micro CT,  
625 *Radiology*, 229 (2003) 921-928.

626 [20] P. Schneider, T. Krucker, E. Meyer, A. Ulmann-Schuler, B. Weber, M. Stampanoni, R.  
627 Müller, Simultaneous 3D visualization and quantification of murine bone and bone  
628 vasculature using micro-computed tomography and vascular replica, *Microsc Res Tech*, 72  
629 (2009) 690-701.

630 [21] P. Schneider, M. Stauber, R. Voide, M. Stampanoni, L.R. Donahue, R. Müller,  
631 Ultrastructural properties in cortical bone vary greatly in two inbred strains of mice as  
632 assessed by synchrotron light based micro- and nano-CT, *J Bone Miner Res*, 22 (2007) 1557-  
633 1570.

634 [22] B. Pouran, V. Arbabi, R.L. Bleys, P. René van Weeren, A.A. Zadpoor, H. Weinans, Solute  
635 transport at the interface of cartilage and subchondral bone plate: Effect of micro-  
636 architecture, *J Biomech*, 52 (2017) 148-154.

637 [23] A. Malandrino, D. Lacroix, C. Hellmich, K. Ito, S.J. Ferguson, J. Noailly, The role of endplate  
638 poromechanical properties on the nutrient availability in the intervertebral disc,  
639 *Osteoarthritis Cartilage*, 22 (2014) 1053-1060.

640 [24] G. Gailani, M. Benalla, R. Mahamud, S.C. Cowin, L. Cardoso, Experimental determination  
641 of the permeability in the lacunar-canalicular porosity of bone, *J Biomech Eng*, 131 (2009)  
642 101007.

643 [25] J. Hwang, W.C. Bae, W. Shieu, C.W. Lewis, W.D. Bugbee, R.L. Sah, Increased hydraulic  
644 conductance of human articular cartilage and subchondral bone plate with progression of  
645 osteoarthritis, *Arthritis Rheum*, 58 (2008) 3831-3842.

646 [26] A. Malandrino, D. Lacroix, C. Hellmich, K. Ito, S.J. Ferguson, J. Noailly, The role of endplate  
647 poromechanical properties on the nutrient availability in the intervertebral disc,  
648 *Osteoarthritis and Cartilage*, 22 (2014) 1053-1060.

649 [27] G.A. Ateshian, The role of interstitial fluid pressurization in articular cartilage lubrication,  
650 *J Biomech*, 42 (2009) 1163-1176.

651 [28] L. Zhang, B.S. Gardiner, D.W. Smith, P. Pivonka, A.J. Grodzinsky, The effect of cyclic  
652 deformation and solute binding on solute transport in cartilage, *Archives of biochemistry and*  
653 *biophysics*, 457 1 (2007) 47-56.

654 [29] S. Miramini, D.W. Smith, L. Zhang, B.S. Gardiner, The spatio-temporal mechanical  
655 environment of healthy and injured human cartilage during sustained activity and its role in  
656 cartilage damage, *J Mech Behav Biomed Mater*, 74 (2017) 1-10.

657 [30] L. Zhang, S. Miramini, D.W. Smith, B.S. Gardiner, A.J. Grodzinsky, Time evolution of  
658 deformation in a human cartilage under cyclic loading, *Ann Biomed Eng*, 43 (2015) 1166-1177.

659 [31] S. Beeler, L. Vlachopoulos, L. Jud, R. Sutter, T. Götschi, P. Fürnstahl, S.F. Fucentese,  
660 Meniscus sizing using three-dimensional models of the ipsilateral tibia plateau based on CT  
661 scans - an experimental study of a new sizing approach, *J Exp Orthop*, 7 (2020) 36.

662 [32] J.M. Marzo, J. Gurske-DePerio, Effects of medial meniscus posterior horn avulsion and  
663 repair on tibiofemoral contact area and peak contact pressure with clinical implications, *Am*  
664 *J Sports Med*, 37 (2009) 124-129.

665 [33] L. Zhang, M. Richardson, P. Mendis, Role of chemical and mechanical stimuli in mediating  
666 bone fracture healing, *Clinical and Experimental Pharmacology and Physiology*, 39 (2012) 706-  
667 710.

668 [34] M.K. Barker, B.B. Seedhom, The relationship of the compressive modulus of articular  
669 cartilage with its deformation response to cyclic loading: does cartilage optimize its modulus  
670 so as to minimize the strains arising in it due to the prevalent loading regime?, *Rheumatology*,  
671 40 (2001) 274-284.

672 [35] L. Zhang, B.S. Gardiner, D.W. Smith, P. Pivonka, A. Grodzinsky, The effect of cyclic  
673 deformation and solute binding on solute transport in cartilage, *Arch Biochem Biophys*, 457  
674 (2007) 47-56.

675 [36] G.A. Ateshian, M.A. Soltz, R.L. Mauck, I.M. Basalo, C.T. Hung, W. Michael Lai, The Role of  
676 Osmotic Pressure and Tension-Compression Nonlinearity in the Frictional Response of  
677 Articular Cartilage, *Transport in Porous Media*, 50 (2003) 5-33.

678 [37] M.A. Soltz, G.A. Ateshian, A Conewise Linear Elasticity mixture model for the analysis of  
679 tension-compression nonlinearity in articular cartilage, *J Biomech Eng*, 122 (2000) 576-586.

680 [38] V.C. Mow, S.C. Kuei, W.M. Lai, C.G. Armstrong, Biphasic creep and stress relaxation of  
681 articular cartilage in compression? Theory and experiments, *J Biomech Eng*, 102 (1980) 73-84.

682 [39] L. Zhang, D.W. Smith, B.S. Gardiner, A.J. Grodzinsky, Modeling the Insulin-Like Growth  
683 Factor System in Articular Cartilage, *PLoS One*, 8 (2013).

684 [40] L. Zhang, Gardiner, Smith, Pivonka, Grodzinsky, On the role of diffusible binding partners  
685 in modulating the transport and concentration of proteins in tissues, *Journal of Theoretical*  
686 *Biology*, 263 (2010) 20--29.

687 [41] L. Zhang, S. Miramini, D.W. Smith, B.S. Gardiner, A.J. Grodzinsky, Time Evolution of  
688 Deformation in a Human Cartilage Under Cyclic Loading, *Annals of Biomedical Engineering*,  
689 43 (2015) 1166-1177.

690 [42] A. Curnier, Q.-C. He, P. Zysset, Conewise linear elastic materials, *Journal of Elasticity*, 37  
691 (1994) 1-38.

692 [43] A. Maroudas, E. Wachtel, G. Grushko, E.P. Katz, P. Weinberg, The effect of osmotic and  
693 mechanical pressures on water partitioning in articular cartilage, *Biochim Biophys Acta*, 1073  
694 (1991) 285-294.

695 [44] S. Treppo, H. Koepp, E.C. Quan, A.A. Cole, K.E. Kuettner, A.J. Grodzinsky, Comparison of  
696 biomechanical and biochemical properties of cartilage from human knee and ankle pairs, *J*  
697 *Orthop Res*, 18 (2000) 739-748.

698 [45] Y. Xia, S. Zheng, A. Bidthanapally, Depth-dependent profiles of glycosaminoglycans in  
699 articular cartilage by microMRI and histochemistry, *J Magn Reson Imaging*, 28 (2008) 151-157.

700 [46] G.E. Kempson, H. Muir, C. Pollard, M. Tuke, The tensile properties of the cartilage of  
701 human femoral condyles related to the content of collagen and glycosaminoglycans, *Biochim*  
702 *Biophys Acta*, 297 (1973) 456-472.

703 [47] L. Zhang, Solute transport in cyclic deformed heterogeneous articular cartilage,  
704 *International Journal of Applied Mechanics*, 3 (2011) 507--524.

705 [48] L. Zhang, B. Gardiner, D. Smith, P. Pivonka, A. Grodzinsky, Integrated model of IGF-I  
706 mediated biosynthesis in a deformed articular cartilage, *Journal of Engineering Mechanics*,  
707 135 (2009) 439--449.

708 [49] L. Zhang, B. Gardiner, D. Smith, P. Pivonka, A. Grodzinsky, A fully coupled poroelastic  
709 reactive-transport model of cartilage, *Molecular & Cellular Biomechanics*, 5 (2008) 133--153.

710 [50] L. Zhang, B. Gardiner, D. Smith, P. Pivonka, A. Grodzinsky, IGF uptake with competitive  
711 binding in articular cartilage, *Journal of Biological Systems*, 16 (2008) 175--195.

712 [51] L. Zhang, B. Gardiner, D. Smith, P. Pivonka, J. Grodzinsky, The effect of cyclic deformation  
713 and solute binding on solute transport in cartilage, *Archives of Biochemistry and Biophysics*,  
714 457 (2007) 47--56.

715 [52] L. Bonassar, A. Grodzinsky, A. Srinivasan, S. Davila, S. Trippel, Mechanical and  
716 Physicochemical Regulation of the Action of Insulin-Like Growth Factor-I on Articular Cartilage,  
717 *Archives of biochemistry and biophysics*, 379 (2000) 57-63.

718 [53] O. Zamparo, W.D. Comper, Hydraulic conductivity of chondroitin sulfate proteoglycan  
719 solutions, *Archives of Biochemistry and Biophysics*, 274 (1989) 259-269.

720 [54] J. Liao, D.W. Smith, S. Miramini, B.S. Gardiner, L. Zhang, A Probabilistic Failure Risk  
721 Approach to The Problem of Articular Cartilage Lubrication, *Computer Methods and Programs*  
722 *in Biomedicine*, 203 (2021) 106053.

723 [55] J. Liao, D.W. Smith, S. Miramini, N. Thibbotuwawa, B.S. Gardiner, L. Zhang, The  
724 investigation of fluid flow in cartilage contact gap, *Journal of the Mechanical Behavior of*  
725 *Biomedical Materials*, 95 (2019) 153-164.

726 [56] J.M. Deneweth, K.E. Newman, S.M. Sylvia, S.G. McLean, E.M. Arruda, Heterogeneity of  
727 tibial plateau cartilage in response to a physiological compressive strain rate, *J Orthop Res*, 31  
728 (2013) 370-375.

729 [57] D.L. Robinson, M.E. Kersh, N.C. Walsh, D.C. Ackland, R.N. de Steiger, M.G. Pandy,  
730 Mechanical properties of normal and osteoarthritic human articular cartilage, *J Mech Behav*  
731 *Biomed Mater*, 61 (2016) 96-109.

732 [58] S. Graindorge, W. Ferrandez, Z. Jin, E. Ingham, C. Grant, P. Twigg, J. Fisher, Biphasic  
733 surface amorphous layer lubrication of articular cartilage, *Medical Engineering & Physics*, 27  
734 (2005) 836-844.

735 [59] J. Martel-Pelletier, D. Lajeunesse, P. Reboul, J.-P. Pelletier, Chapter 2 - The Role of  
736 Subchondral Bone in Osteoarthritis, in: L. Sharma, F. Berenbaum (Eds.) *Osteoarthritis*, Mosby,  
737 Philadelphia, 2007, pp. 15-32.

738 [60] S. Milz, R. Putz, Quantitative morphology of the subchondral plate of the tibial plateau,  
739 *Journal of anatomy*, 185 ( Pt 1) (1994) 103-110.

740 [61] D. Lacroix, P.J. Prendergast, A mechano-regulation model for tissue differentiation during  
741 fracture healing: analysis of gap size and loading, *J Biomech*, 35 (2002) 1163-1171.

742 [62] X. Liu, S. Miramini, M. Patel, J. Liao, D. Shidid, L. Zhang, Influence of therapeutic grip  
743 exercises induced loading rates in distal radius fracture healing with volar locking plate  
744 fixation, *Computer Methods and Programs in Biomedicine*, 215 (2022) 106626.

745 [63] D.W. Goodwin, Y.Z. Wadghiri, H. Zhu, C.J. Vinton, E.D. Smith, J.F. Dunn, Macroscopic  
746 structure of articular cartilage of the tibial plateau: influence of a characteristic matrix  
747 architecture on MRI appearance, *AJR Am J Roentgenol*, 182 (2004) 311-318.

748 [64] M.A.J. Finnilä, J. Thevenot, O.M. Aho, V. Tiitu, J. Rautiainen, S. Kauppinen, M.T. Nieminen,  
749 K. Pritzker, M. Valkealahti, P. Lehenkari, S. Saarakkala, Association between subchondral bone  
750 structure and osteoarthritis histopathological grade, *J Orthop Res*, 35 (2017) 785-792.

751 [65] H.L. Stewart, C.E. Kawcak, The Importance of Subchondral Bone in the Pathophysiology  
752 of Osteoarthritis, *Front Vet Sci*, 5 (2018) 178.

753 [66] I. Kutzner, B. Heinlein, F. Graichen, A. Bender, A. Rohlmann, A. Halder, A. Beier, G.  
754 Bergmann, Loading of the knee joint during activities of daily living measured in vivo in five  
755 subjects, *J Biomech*, 43 (2010) 2164-2173.

756 [67] C.E. Metzger, D.B. Burr, M.R. Allen, Anatomy and Structural Considerations, in: M. Zaidi  
757 (Ed.) *Encyclopedia of Bone Biology*, Academic Press, Oxford, 2020, pp. 218-232.

758 [68] K. Rogers, *Encyclopedia Britannica*, The Editors of Encyclopaedia Britannica, 2015.

759 [69] X. Zhu, Y.T. Chan, P.S.H. Yung, R.S. Tuan, Y. Jiang, Subchondral Bone Remodeling: A  
760 Therapeutic Target for Osteoarthritis, *Front Cell Dev Biol*, 8 (2020) 607764.

761 [70] H. Madry, C.N. van Dijk, M. Mueller-Gerbl, The basic science of the subchondral bone,  
762 *Knee Surg Sports Traumatol Arthrosc*, 18 (2010) 419-433.

763 [71] A. Hosseini, S.K. Van de Velde, M. Kozanek, T.J. Gill, A.J. Grodzinsky, H.E. Rubash, G. Li,  
764 In-vivo time-dependent articular cartilage contact behavior of the tibiofemoral joint,  
765 *Osteoarthritis Cartilage*, 18 (2010) 909-916.

766 [72] G.A. Ateshian, A theoretical formulation for boundary friction in articular cartilage, *J*  
767 *Biomech Eng*, 119 (1997) 81-86.

768 [73] R. Krishnan, M. Kopacz, G.A. Ateshian, Experimental verification of the role of interstitial  
769 fluid pressurization in cartilage lubrication, *J Orthop Res*, 22 (2004) 565-570.

770 [74] H. Forster, J. Fisher, The Influence of Loading Time and Lubricant on the Friction of  
771 Articular Cartilage, *Proceedings of the Institution of Mechanical Engineers, Part H: Journal of*  
772 *Engineering in Medicine*, 210 (1996) 109-119.

773 [75] M.J. Carter, I.M. Basalo, G.A. Ateshian, The temporal response of the friction coefficient  
774 of articular cartilage depends on the contact area, *J Biomech*, 40 (2007) 3257-3260.

775 [76] A. Oloyede, N.D. Broom, Is classical consolidation theory applicable to articular cartilage  
776 deformation?, *Clin Biomech (Bristol, Avon)*, 6 (1991) 206-212.

777 [77] B. Li, D. Marshall, M. Roe, R.M. Aspden, The electron microscope appearance of the  
778 subchondral bone plate in the human femoral head in osteoarthritis and osteoporosis, *J Anat*,  
779 195 ( Pt 1) (1999) 101-110.

780 [78] S. Shimizu, Y. Asou, S. Itoh, U.I. Chung, H. Kawaguchi, K. Shinomiya, T. Muneta, Prevention  
781 of cartilage destruction with intraarticular osteoclastogenesis inhibitory  
782 factor/osteoprotegerin in a murine model of osteoarthritis, *Arthritis Rheum*, 56 (2007) 3358-  
783 3365.

784 [79] S.K. Tat, J.P. Pelletier, C.R. Velasco, M. Padrines, J. Martel-Pelletier, New perspective in  
785 osteoarthritis: the OPG and RANKL system as a potential therapeutic target?, *Keio J Med*, 58  
786 (2009) 29-40.

787 [80] A.R. Upton, C.A. Holding, A.A. Dharmapatni, D.R. Haynes, The expression of RANKL and  
788 OPG in the various grades of osteoarthritic cartilage, *Rheumatol Int*, 32 (2012) 535-540.

789 [81] B. Bolon, M. Grisanti, K. Villasenor, S. Morony, U. Feige, W.S. Simonet, Generalized  
790 Degenerative Joint Disease in Osteoprotegerin (Opg) Null Mutant Mice, *Vet Pathol*, 52 (2015)  
791 873-882.

792 [82] B. Kovács, E. Vajda, E.E. Nagy, Regulatory Effects and Interactions of the Wnt and OPG-  
793 RANKL-RANK Signaling at the Bone-Cartilage Interface in Osteoarthritis, International Journal  
794 of Molecular Sciences, 20 (2019) 4653.  
795 [83] F. Boschetti, G.M. Peretti, M. Colombo, S. Cattaneo, R. Pietrabissa, F. Gervaso, G.  
796 Fraschini, Direct and indirect measurement of human articular cartilage permeability, 2004.  
797 [84] S.M. McNary, K.A. Athanasiou, A.H. Reddi, Engineering lubrication in articular cartilage,  
798 Tissue Eng Part B Rev, 18 (2012) 88-100.  
799

**Title: Osteochondral junction leakage and cartilage joint lubrication**

Qin Li

Department of Infrastructure Engineering,  
The University of Melbourne, Victoria 3010, Australia  
Email: [qinl3@student.unimelb.edu.au](mailto:qinl3@student.unimelb.edu.au)

Dr Saeed Miramini

Department of Infrastructure Engineering,  
The University of Melbourne, Victoria 3010, Australia  
Email: [s.miramini@unimelb.edu.au](mailto:s.miramini@unimelb.edu.au)

Professor David Smith

School of Physics, Mathematics and Computing,  
The University of Western Australia, WA 6009, Australia  
Email: [David.smith@uwa.edu.au](mailto:David.smith@uwa.edu.au)

Professor Bruce Gardiner

Centre for Molecular Medicine and Innovative Therapeutics  
Murdoch University, WA 6150, Australia  
Email: [B.Gardiner@murdoch.edu.au](mailto:B.Gardiner@murdoch.edu.au)

Professor Lihai Zhang

Department of Infrastructure Engineering,  
The University of Melbourne, Victoria 3010, Australia  
Email: [lihzhang@unimelb.edu.au](mailto:lihzhang@unimelb.edu.au)